PCCP

Accepted Manuscript

ROYAL SOCIETY OF CHEMISTRY

www.rsc.org/pccp

ARTICLE TYPE www. rsc.org/xxxxxx | XXXXXXXX

Molecular collisions coming into focus

Jolijn Onvlee,[a] Sjoerd N. Vogels,[a] Alexander von Zastrow, [a] David H. Parker [a] and Sebastiaan Y.T. van de Meerakker*[a]

Received Xth XXXXXXXXXX 20XX, Accepted Xth XXXXXXXXX 20XX
First published on the web Xth XXXXXXXXXX 200X
DOI: 10.1039/b000000x

The Stark deceleration method exploits the concepts of charged particle accelerator physics to produce beams of neutral polar molecules with an almost perfect quantum state purity, a tunable velocity and a narrow velocity distribution. These monochromatic molecular beams offer interesting perspectives for precise studies of molecular scattering processes, in particular when used in conjunction with state-of-the-art laser-based detection techniques such as velocity map imaging. Here, we describe crossed beam scattering experiments in which the Stark deceleration method is combined with the velocity map imaging technique. The narrow velocity spread of Stark-decelerated molecular beams results in scattering images with unprecedented velocity and angular resolution. We demonstrate this by resolving quantum diffraction oscillations in state-to-state inelastic differential scattering cross sections for collisions between NO radicals and rare gas atoms. We describe the future prospects of this "best-of-two-worlds" combination, ranging from scattering studies at low collision energies to bimolecular scattering using two decelerators, and discuss the challenges that lie ahead to achieve these goals.

1 Introduction

The study of collisions between molecules in the gas-phase is a well-established approach to probe the potential energy surfaces that govern molecular interactions, and has a long and rich history in physical chemistry. The level of detail that can be obtained in these studies depends both on the quality of preparation of the collision partners before the collision, and on how accurately the products are analyzed afterwards. As Raphael Levine and Richard Bernstein wrote in their classic book "Molecular Reaction Dynamics and Chemical Reactivity"[1]: "In the ultimate experiment one would determine the cross section and angular distribution of the products for a completely specified collision". The parameters that are to be specified can be roughly divided into two categories. The parameters in the first category refer to the pre-collision conditions of the reagent atoms and molecules, and include the internal quantum state, the alignment or orientation, and the energy of the collision. The second category contains the post-collision properties of the products, such as quantum state, alignment or orientation, and velocity. For favorable systems, (vector)correlations between several pre- and post-collision parameters can even be determined[2].

Experimentally, collision events can be most precisely specified when crossed atomic and molecular beams are used to produce intense jets of particles, confined to a few quantum states[3]. The crossed molecular beams technique enables the study of molecular encounters under single collision conditions, and has been established as an important and mature method[4–6]. A rich variety of geometries has been engineered to obtain further control over the reagent's pre-collision parameters. These methods either rely on inventive crossed beam geometries, or actively manipulate molecules in the beam using electric, magnetic, or optical fields[7–9]. Equally impressive progress has been made to probe the collision products. Ingenious laser-based detection methods have been developed to measure the state, angular, and velocity distributions of the molecules after the collision[10–13].

Despite these successes, major challenges still exist, in particular in our understanding of scattering systems that involve more than just a few atoms. Scattering cross sections for collisions between an atom and a diatomic molecule can now be calculated at the full quantum state level routinely in excellent agreement with experiments, however, much less is known about inelastic or reactive processes for larger and more complex systems. This is particularly true for collisions involving open-shell species that are governed by multiple Born-Oppenheimer potential energy surfaces with non-adiabatic couplings between them. For these systems, experimental validation of theoretical models is essential. Therefore, the quest for obtaining experimental collision data with the highest possible accuracy and precision is just as important today as it was when Levine and Bernstein wrote their book in the 1980's.

During the last 15 years, two techniques have been developed – one in each parameter category – that yield new possibilities and prospects to study molecular collisions. The first development has been the invention of the velocity map

[a] *Radboud University Nijmegen, Institute for Molecules and Materials, Heijendaalseweg 135, 6525 AJ Nijmegen, the Netherlands*

imaging (VMI) technique by Parker and coworkers [14], which has been an important improvement for our ability to probe collision products. Using VMI, the velocity vectors of scattered molecules in the plane of the crossed beams can be directly imaged onto a position sensitive detector, thereby probing all product recoil angles simultaneously. In combination with laser-based state-specific ionization methods, this offers the revolutionary capability to generate images of recoiling molecules that directly reflect the state-resolved differential cross section (DCS). This opened new avenues in molecular collision research and yielded information on scattering processes that were inconceivable only a few years ago [11].

The second technique is the Stark deceleration method developed by Meijer and coworkers, which has been a significant advance in our ability to manipulate molecular beams [15,16]. The Stark decelerator is an analogue of a linear accelerator (LINAC) for charged particles, and allows for the deceleration or acceleration of neutral polar molecules to any desired velocity, while keeping them together as a compact packet. These tamed molecular beams offer a tunable velocity, narrow velocity and angular spreads, narrow spatial distributions, (almost) perfect quantum state purity, and a high degree of spatial orientation [17]. Clearly, these beams are an excellent starting point for precise molecular collision experiments [18–20].

With VMI detectors now readily available at reasonable cost, VMI has been implemented in many laboratories in recent years. The application of Stark-decelerated molecular beams in scattering experiments, however, is still in its infancy. Yet, for specific systems, these tamed molecular beams are ideally suited to mitigate the major bottleneck that currently limits the resolution in crossed beam experiments: the quality of the molecular beam pulses. The collision partners generated by conventional beam sources have relatively broad velocity distributions, and reagents usually populate several quantum states. Even using the most sophisticated beam preparation techniques, the overlap between the signals from collision partners with different velocities and internal energy may blur the detailed structures in cross sections that are predicted by theory.

Recently, we reported the first crossed beam scattering experiment in which a Stark decelerator was combined with VMI [21]. This best-of-both-worlds combination resulted in scattering images with extremely high velocity and angular resolution. This was illustrated by resolving quantum diffraction oscillations in state-to-state DCSs for inelastic scattering between state-selected NO radicals and rare gas (Rg) atoms, which serves as a benchmark system for rotational energy transfer [22]. These quantum diffraction oscillations are among the most detailed structures that can occur in any DCS.

In this manuscript, we give a detailed account of the experimental arrangement used to obtain these high resolution scattering images and we describe the future prospects of scattering experiments that employ both deceleration and imaging techniques. For this, we use specific case studies as an example. These include the possibility of studying low collision energy phenomena, and the measurement of product pair correlations for the scattering of two state-selected molecules. We describe the challenges that need to be overcome to obtain these goals, and give our opinion on the advantages and limitations of the approach.

2 Experiment

2.1 Experimental set-up

A schematic overview of the Nijmegen crossed beam set-up is shown in Figure 1. A pulsed supersonic beam of NO radicals is produced by expanding 2% NO seeded in an inert carrier gas through a Nijmegen pulsed valve [23]. This valve produces a beam pulse with a temporal duration of about 25 μs (full width at half maximum (FWHM)). The carrier gases Xe and Kr are used to produce beams with a mean velocity between 350 and 550 m/s. During the expansion, nearly all NO radicals cool to the lowest rotational ($j = 1/2$) and vibrational level of the $X\,^2\Pi_{1/2}$ electronic ground state.

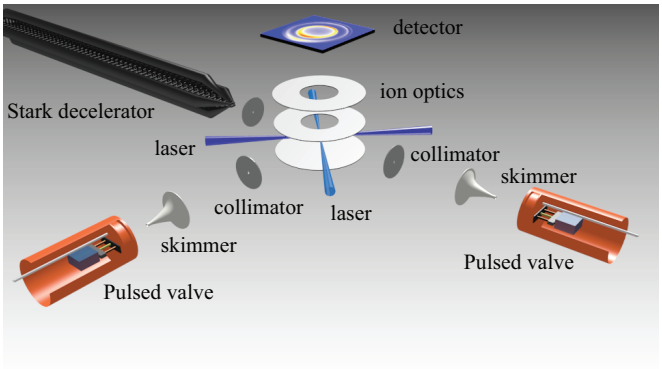

Fig. 1 Schematic representation of the experimental set-up. A pulsed beam of NO radicals is passed through a 2.6-meter long Stark decelerator, and is scattered with a pulsed beam of rare gas atoms. The inelastically scattered NO radicals are state-selectively ionized using two pulsed lasers, and detected using velocity map imaging. Only the last section of the Stark decelerator is shown.

After passage through a 3 mm diameter skimmer, the beam enters the 2.6-meter long Stark decelerator that consists of 317 pairs of high-voltage electrodes [24]. The operation and characterization of a Stark decelerator has been described in detail before [17], and will not be repeated here. The Stark decelerator is operated in the $s = 3$ mode using a phase angle $\phi_0 = 0°$ throughout [25], and a voltage difference of 36 kV is applied between opposing electrodes. A detailed description of the NO packet that exits the Stark decelerator will be given in section

2.2.

The packet of NO radicals intersects with the central axis of a beam of Rg atoms at a distance of 72 mm from the exit of the decelerator. Two conventional molecular beams are installed at crossing angles of 90° and 180°, respectively. This allows for measurements of collisions between Stark-decelerated molecules and Rg atoms at both crossing angles, but also enables crossed beam experiments using conventional beams only. Both beam sources are located 110 mm from the interaction region. For both beams, a 2 mm diameter skimmer is mounted at a distance of 87 mm from the interaction region in a conically shaped and differentially pumped source chamber. The beam containing the collision partner is produced by expanding neat Ne or Ar with a backing pressure of typically 3 bars into vacuum using a commercially available pulsed valve (Jordan Inc.).

The collision region itself is surrounded by an octagonal structure that is mounted in the center of the collision chamber. Figure 2 shows a photograph of the top view of the interaction region with the last section of the decelerator, the two conically shaped source chamber walls, and the octagonal structure. Collimators with different diameters can be precisely mounted in the eight faces of the octagon, such that the axes that connect the centers of opposing collimators exactly coincide with the center of the octagon. The three molecular beams are aligned such that the beam axis passes through the center of a collimator. The octagonal structure allows for an easy and reproducible exchange of collimators with different hole diameters, and ensures that all molecular and laser beams are properly aligned. In all experiments reported here, collimators with a 3 mm diameter are used.

For the detection of the NO molecules, two pulsed dye laser systems are used. The first laser is used to excite NO radicals to the electronically excited $A\,^2\Sigma^+$ state by inducing the $(0-0)$ band of the $A\,^2\Sigma^+ \leftarrow X\,^2\Pi$ transition. The 226 nm radiation with a bandwidth of approximately 0.08 cm^{-1}, a 5 ns pulse duration and a 3 mm diameter is produced by frequency tripling the output of a Nd:YAG laser pumped dye laser. The second dye laser (328 nm, bandwidth approximately 0.06 cm^{-1}, 5 ns pulse duration, 4 mm diameter) is pumped by another Nd:YAG laser, and is used to subsequently ionize the NO radicals just above the energetic threshold. Both laser beams are fired in the plane of the molecular beams, and cross each other under 90°, as indicated in Figure 2. They are both focused into the scattering volume to offer a small ionization volume. The first and second color are attenuated to 3 μJ and 6 mJ, respectively, to prevent Coulomb repulsion effects from excessive signal levels and to prevent direct (1+1) resonance enhanced multi-photon ionization (REMPI) by the first dye laser only. It is verified that all ionization signal disappears when blocking either of the two laser beams.

The VMI electric field geometry is produced by ion optics

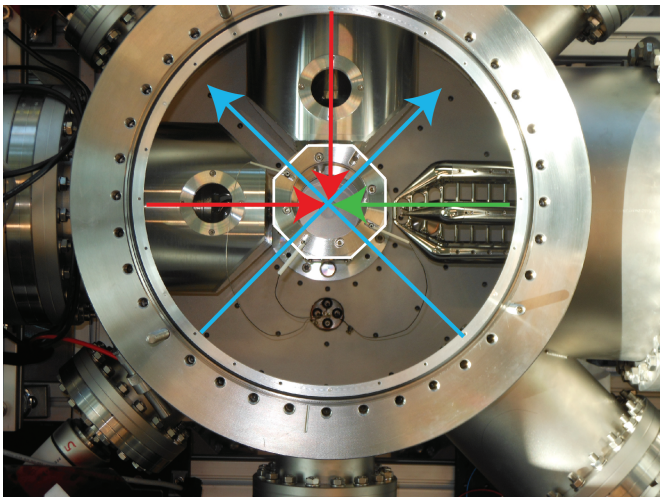

Fig. 2 Photograph of the top view of the interaction region, showing two conically shaped differentially pumped chambers in which the two conventional beams are produced (left and top), the final section of the Stark decelerator (right), and the octagonal structure that surrounds the interaction region (white). The arrows indicate the propagation directions of the Stark-decelerated beam (green), the two conventional molecular beams (red), and the two laser beams (blue).

that consists of a repeller, an extractor and grounded plate. The assembly is suspended in the octagonal structure such that the 20 mm diameter hole in the extractor plate is precisely centered above the interaction region. Voltages of 1000 V and 758 V are applied to the repeller and extractor plates, respectively, to ensure velocity mapping conditions. Ions pass through a grounded time-of-flight tube of 550 mm length before impinging on a microchannel plate detector that is coupled to a phosphor screen. No time-slicing is available in the present arrangement. Images are recorded using a CCD camera (PCO Pixelfly 270XS, 1391×1023 pixels), and transferred to a PC for subsequent averaging and data analysis. Scattering images are recorded by first overlapping both the atomic and molecular beams in time and then delaying the Rg atom beam with respect to the NO packet, such that only background signals are recorded. This is done in an alternating fashion and the final scattering image is inferred from the signal intensity difference of both images. Event counting, and a similar centroiding algorithm as described by Suits and coworkers[26], are used in the data acquisition software to obtain sub-pixel velocity resolution. All pixel numbers in this manuscript refer to sub-pixels, where every pixel of the camera is divided into four sub-pixels.

2.2 The reagent packet of NO radicals

The manipulation of NO radicals in a Stark decelerator has been presented recently[27]. Here, we describe only the aspects that are most relevant to scattering experiments, and present a detailed characterization of the packet of NO that emerges from the decelerator.

The energy level scheme of NO in the $X\,^2\Pi_{1/2}$ electronic ground state is shown in Figure 3*a*. Each rotational state consists of two Λ-doublet components, where the lower and upper components are of *e* and *f* parity, respectively. For the $j = 1/2$ rotational ground state, the Λ-doublet splitting amounts to 318 MHz, and both components are equally populated in the molecular beam. Figure 3*b* shows the Stark shift of the $j = 1/2$ state. The hyperfine structure has been neglected in this figure, and is not relevant to the experiments reported here. It can be seen that only molecules that reside in the energetically higher lying *f*-component are low field seeking in inhomogeneous electric fields, and can be manipulated inside the Stark decelerator. Molecules in the lower *e*-component are high field seeking and are therefore deflected from the beam axis in the experiment.

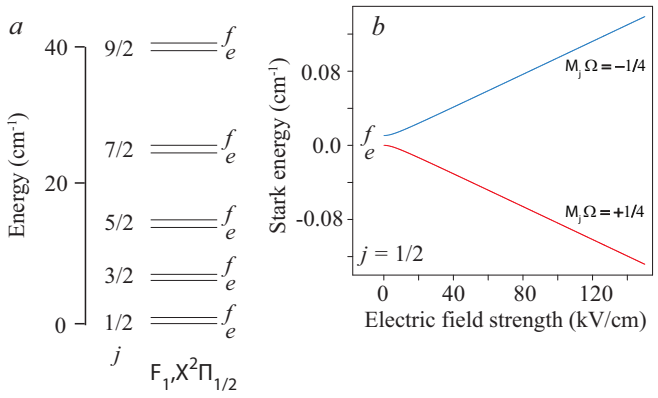

Fig. 3 (a) Energy level diagram of NO, where the energy splitting between the Λ-doublet components of each rotational level is greatly exaggerated for clarity. (b) The Stark shift of NO radicals in the $X\,^2\Pi_{1/2}, j = 1/2$ state as function of the electric field strength. The low-field seeking component of *f* parity and the high-field seeking component of *e* parity are indicated by the blue and red curve, respectively.

The electric dipole moment of NO is only 0.16 D, hence NO radicals in the $X\,^2\Pi_{1/2}, j = 1/2, f$ state cannot be significantly accelerated or decelerated in our Stark decelerator. Instead, we use the decelerator to select a fraction of the molecular beam pulse with a narrow velocity distribution, and guide this fraction through the decelerator at constant velocity. Figure 4*a* shows a time-of-flight (TOF) profile of NO $X\,^2\Pi_{1/2}, j = 1/2, f$ radicals exiting the Stark decelerator which is programmed to select a packet with a mean velocity of 480 m/s. In this figure, time-of-flight refers to the time at which the first electrodes of the decelerator are switched to high voltage, i.e., when the molecular beam arrives at the entrance of the Stark decelerator. The selected packet results in a narrow and intense central peak in the TOF profile at an arrival time of about 5.58 ms, with a width of 14 μs (FWHM). The wings of the TOF profile contain the remainder of the molecular beam pulse. The sharp features that are visible on either side of the central peak have been observed and interpreted before[28].

The TOF profile that results from a three dimensional trajectory simulation of the experiments, following the methods described by Van de Meerakker *et al.*[28], is shown underneath the experimental TOF profile in Figure 4*a*. The simulated profile is in excellent agreement with the experimentally observed profile. From these trajectory simulations we can derive the velocity and spatial distributions of the selected NO packet that emerges from the decelerator. The longitudinal and transverse velocity distributions are shown in Figures 4*b* and *c*, respectively. The spatial distributions are shown in Figures 4*d* and *e*. The longitudinal and transverse velocity distributions do not follow a Gaussian distribution, but have sharp cut-offs on both wings of the distribution. The distribution has a width (FWHM) of 2.8 m/s and 0.6 m/s in the longitudinal and transverse direction, respectively. The velocity distribution can also be expressed as a speed ratio of $S = 404$ (or a temperature of $T = 5.1$ mK) and a divergence of 0.07° for the packet of NO molecules. We define the speed ratio S as $S = v/\Delta v$ and the temperature T as $T = m\Delta v^2/k_B$, where Δv is the longitudinal velocity spread (σ) of the velocity distribution, m the mass of the NO molecule, and k_B the Boltzmann constant. The packet is also well defined spatially, with a width (FWHM) of approximately 6 mm and 1 mm in the longitudinal and transverse direction, respectively.

The mean velocity and velocity distributions of the NO packet can also be measured using VMI, as shown in Figure 2 of ref.[21], in which a VMI image is shown of the reagent packet of NO $X\,^2\Pi_{1/2}, j = 1/2, f$ molecules. We refer to such images of the reagent packet of NO as beam spot. For our experimental set-up, each sub-pixel corresponds to a velocity of 1.2 m/s (see section 2.3), and the size of the measured beam spot is consistent with the velocity distributions that are inferred from the trajectory simulations.

The manipulation of molecules inside a Stark decelerator results in high quantum state purities of the emerging packet of molecules. Figure 5 shows a REMPI spectrum of the NO packet. The vast majority of the NO radicals resides in the $j = 1/2, f$ level and only a minor fraction is observed in the $j = 3/2, f$ level. Although the $j = 1/2, e$ and $j = 1/2, f$ levels are equally populated in the molecular beam pulse, the population in the *e* level is diminished to neglectable values by the Stark decelerator.

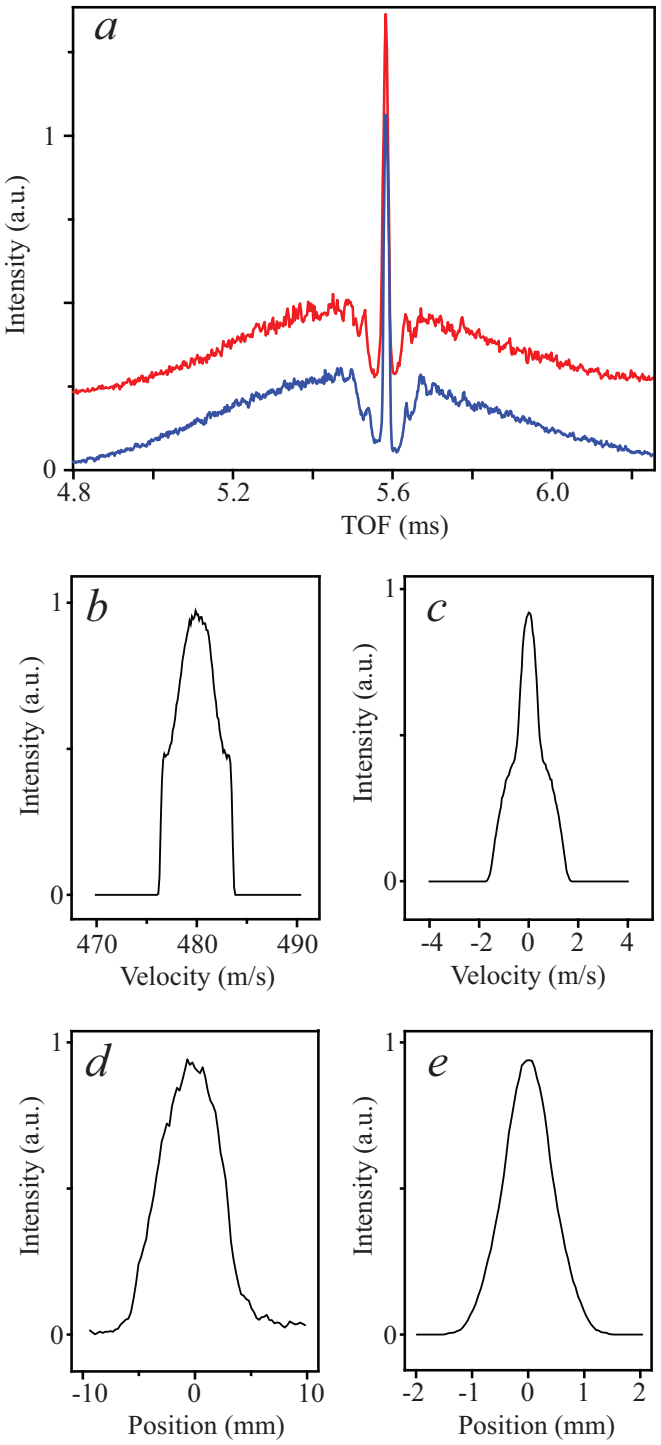

Fig. 4 (a) Experimental (red) and simulated (blue) TOF profiles of NO $X\,^2\Pi_{1/2}, j = 1/2, f$ radicals exiting the decelerator with a mean velocity of 480 m/s. Both curves are given a vertical offset for reasons of clarity. (b) Longitudinal velocity distribution, (c) transverse velocity distribution, (d) longitudinal spatial and (e) transverse spatial distribution of the NO packet exiting the Stark decelerator.

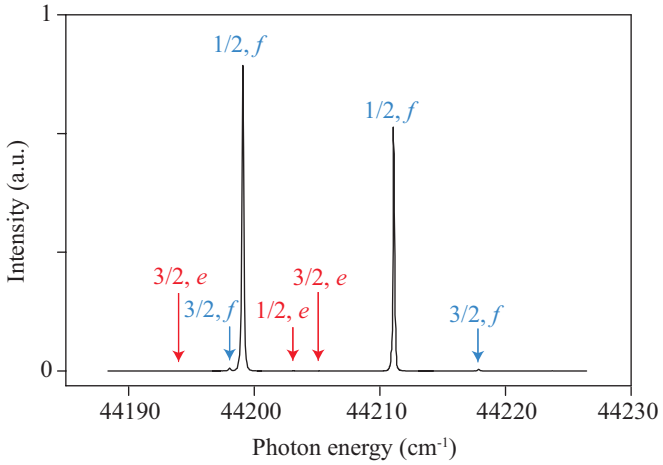

Fig. 5 Experimental REMPI spectrum of the NO packet exiting the Stark decelerator. The labels indicate the rotational levels from which the transitions originate. The red and blue colors specify the high-field seeking states of e parity, and the low-field seeking states of f parity, respectively. Molecules in high-field seeking states are deflected from the beam axis inside the Stark decelerator, and hardly contribute to the spectrum.

2.3 Detector calibration

For the interpretation and analysis of scattering images, an accurate calibration of the VMI detector is essential. The conversion factor that relates camera pixels to actual velocities is usually determined by measuring the diameter of an image for a photodissociation process, for which the recoil energy is accurately known. This, however, can be a time-consuming and cumbersome task. In our experiment, the Stark decelerator produces packets of molecules with an extremely well known mean velocity that is set by the sequence of high voltage pulses applied to the decelerator. We use this knowledge to accurately calibrate the detector by selecting packets of NO with a velocity ranging from 350 to 550 m/s from the molecular beam pulse. The resulting beam spot images are shown in Figure 6*a*. The mean impact positions on the detector are determined for all beam spots. These positions are shown in panel *b* and *c* for the directions along and perpendicular to the propagation direction of the Stark decelerated beam, respectively. A linear relation between the mean velocity of the NO packet and the mean impact position is observed, directly yielding a pixel-to-m/s conversion factor of 1.2 m/s per pixel for the current set-up. In our case, the camera would ideally be positioned such that the two orthogonal axes defining the pixel grid of the camera coincide with the two orthogonal beam propagation directions. We nearly accomplished this situation; the beam spots are displaced by only about two pixels in the direction transverse to the NO propagation direction over the velocity range that is probed.

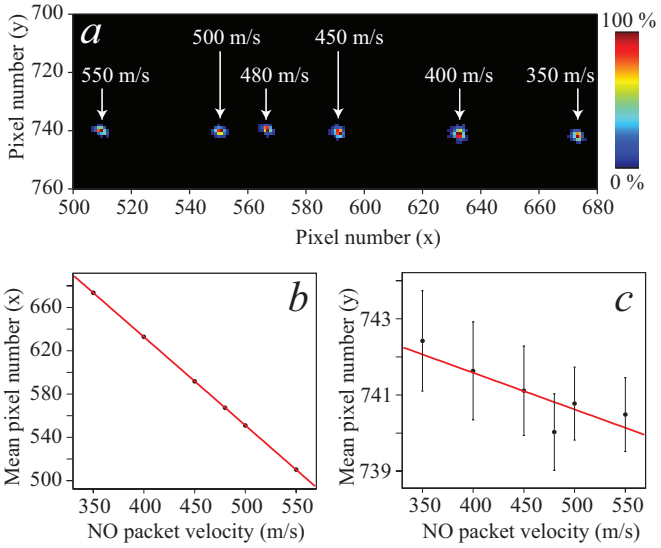

Fig. 6 (a) Image showing the beam spots of NO packets that emerge from the Stark decelerator with a velocity ranging from 350 to 550 m/s. The mean impact positions (in pixel units) of these beam spots are plotted as function of the mean velocity for the directions along (b) and perpendicular (c) to the propagation direction of the Stark-decelerated beam. Note the different vertical scales that were used in panel (b) and (c).

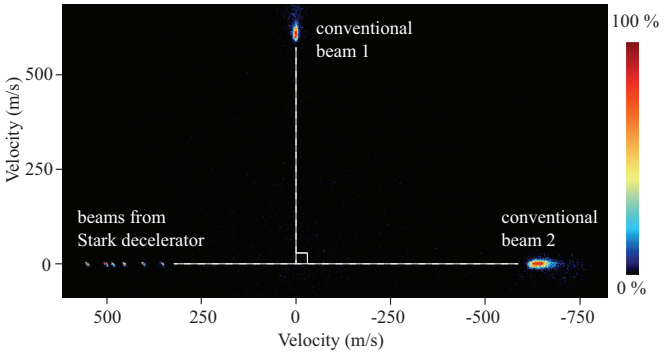

Fig. 7 Beam spots of NO radicals that emerge from the Stark decelerator or that originate from either of the two conventional molecular beam sources. The mean positions of the spots are converted into velocities using the detector calibration as illustrated in Figure 6. The two orthogonal lines define the laboratory zero-velocity origin of the detector. Note the much larger velocity spreads for the NO radicals entrained in the conventional beams compared to the NO radicals that have passed through the Stark decelerator.

The curves as shown in Figure 6*b* can be extrapolated to zero velocity, yielding the point on the detector that corresponds to stationary molecules in the laboratory frame. With our experimental arrangement, we have a second independent method to determine this zero-velocity origin. This is illustrated in Figure 7. First, a series of beam spots is measured for NO packets that emerge from the Stark-decelerator, similar to the measurement presented in Figure 6. Then the two beam spots are measured that originate from the two conventional beams, which both contain trace amounts of NO molecules. Two orthogonal lines are subsequently fit to the mean impact positions, reflecting the experimental geometry of the beams. Assuming perfect alignment of the beams with respect to each other, i.e., a 90° and 180° crossing angle between the Stark decelerator and the beam axes of the two conventional beams, the zero-velocity origin is directly obtained from the crossing point of the two orthogonal lines. The origins that are found using both methods coincide within a few pixels.

The detector calibration methodology outlined above is fast and very reproducible. When accumulating scattering data, it is typically repeated several times a day to account for a slow drifting of voltages or charging effects.

3 Results and Discussion

3.1 Imaging collisions with improved resolution

To illustrate the high image resolution afforded by the Stark decelerator, Figure 8 shows two images obtained for scattering into the $X\,^2\Pi_{1/2}, j = 7/2, e$ state for NO + Ar collisions as an example. The image shown in panel *a* results when the parent NO radicals are produced using one of the conventional beams, and scatter with a beam of Ar atoms from the other conventional beam source. The image shown in panel *b* is taken when the NO beam passes through the Stark decelerator before it scatters with a conventional beam of Ar. We refer to these images as conventional image and high-resolution image, respectively. In panel *c*, the vector (Newton) diagram is shown that defines the NO, Ar, center-of-mass and relative velocities. Scattering images are presented such that the mean relative velocity (REL) is always oriented horizontally. Both the mean initial NO and Ar velocities were slightly different when recording these two images, resulting in a slightly larger ring radius for the image shown in panel *a*.

The increased resolution that is obtained when a Stark-decelerated beam rather than a conventional beam is used, is evident. The conventional image, although of high-quality for the scattering process measured here, features a relatively broad ring. At scattering angles around forward scattering, the image is distorted due to initial population of NO radicals in the $j = 7/2, e$ state, as is frequently observed in scattering im-

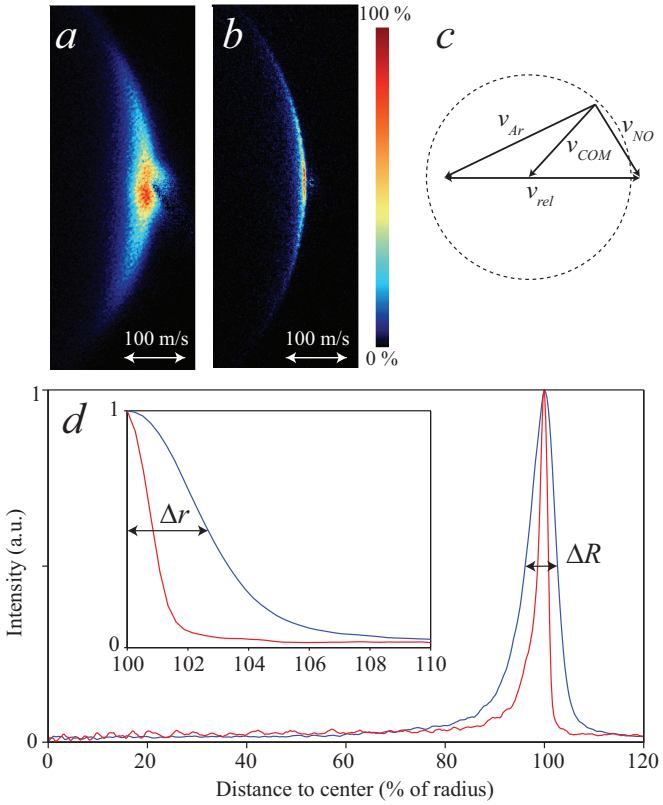

Fig. 8 Velocity mapped ion images for the scattering process NO($j = 1/2, f$) + Ar → NO($j = 7/2, e$) + Ar that are obtained when (a) the parent NO beam is generated using a conventional beam source and (b) when the parent NO radicals are passed through the Stark decelerator. (c) Newton diagram for the scattering images, defining the NO, Ar, center-of-mass (COM) and relative (REL) velocities. (d) Radial intensity distributions of the conventional (blue) and high-resolution (red) images for angular sections of $\Delta\theta = 15°$. The radii of the two images at which the highest intensities are found are normalized to each other.

ages. The high-resolution image, in contrast, is much sharper and is hardly affected by the unwanted beam spot at forward scattering angles.

It should be noted that both images display a different scattering process, however. Whereas both Λ-doublet components of the $j = 1/2$ rotational ground state of NO are equally populated in the conventional beam, the packet of NO that emerges from the decelerator exclusively resides in the upper Λ-doublet component of f parity. This will result in an inherently different DCS when probing the $j = 7/2, e$ state. We therefore refrain from extracting DCSs from the images, but only analyze the difference in sharpness of the images, i.e., the radial resolution.

In Figure 8*d*, the radial intensity distributions of both the conventional (blue curve) and high-resolution (red curve) images are shown for angular sections $\Delta\theta = 15°$, taken in parts of the images that are not distorted from the parent beam spot. The highest intensity in the conventional and high-resolution images is found at a radius of 462 m/s and 448 m/s, respectively, reflecting the slight difference in collision energy for both measurements. To facilitate a direct comparison of the radial intensity distributions, the radii at which the highest intensities are found are normalized to each other. The conventional and high-resolution images have full radial widths ΔR of 30 m/s and 9.6 m/s as defined in the image and the outer rims of the images have radial widths Δr of 12 m/s and 3.6 m/s, respectively.

3.2 Diffraction oscillations

In addition to the radial resolution, the angular resolution of the images determines how well detailed structures in DCSs can be resolved in the experiment. Figure 9*a* shows a typical image that is recorded for NO + Ne collisions, probing the final state $j = 3/2, e$[21]. The angular resolution in this image is clearly sufficient to resolve diffraction oscillations in the state-to-state DCS, as illustrated in the enlarged view of the image in panel *b*. These oscillations originate from quantum interference of different trajectories of the colliding particles on the underlying PES, resulting in the same deflection angle.

The oscillatory diffraction structure is appraised best by a three-dimensional representation of the data shown underneath the two-dimensional images. A small segment of the distribution around forward scattering is masked by trace amounts of the reagent NO packet. Figure 9*d* shows the corresponding three-dimensional representation of the angular scattering distribution that results from a simulation of the experiment. This simulation is based on the temporal, spatial and velocity distributions of both beams, as well as on the spatial overlap of the laser beams with the scattering volume, and it uses the DCS predicted by high level quantum mechanical close-coupling (QM CC) calculations as input[21].

The angular scattering intensity distributions derived from both the experimental (red curve) and simulated images (black curve) are shown in Figure 9*e*. We use the convention that $\theta = 0°$ and $\theta = 180°$ correspond to forward and backward scattering, respectively. Figure 9*f* shows these angular distributions for scattering between NO and Ar, probing the $j = 7/2, e$ state. This demonstrates that we can even resolve diffraction oscillations for systems with a relatively high reduced mass and for higher final rotational levels. The experimentally observed angular scattering distributions are in very good agreement with the DCSs predicted by QM CC calculations. The broader envelope structures in the DCS with superimposed rapid diffraction oscillations are almost perfectly reproduced by the simulations.

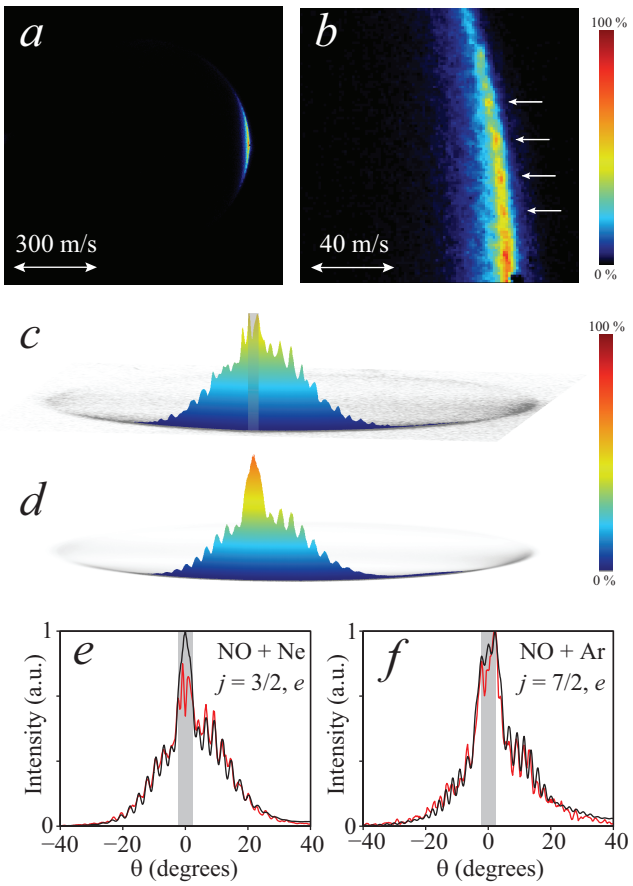

Fig. 9 Scattering distributions for NO + Ne and NO + Ar collisions revealing quantum diffraction oscillations. (a) Raw experimental ion image for the scattering process NO ($j = 1/2, f$) + Ne → NO ($j = 3/2, e$) + Ne. (b) Enlarged view of part of the image, revealing a rapid oscillatory structure in the angular scattering distribution. (c) Three-dimensional representation of the experimental data. (d) Three-dimensional representation of the angular scattering distribution derived from a simulation of the experiment, that is based on a theoretical prediction for the differential cross section. (e and f) Experimentally determined angular scattering distributions (red curves) for the scattering processes NO ($j = 1/2, f$) + Ne → NO ($j = 3/2, e$) + Ne (panel (e)) and NO ($j = 1/2, f$) + Ar → NO ($j = 7/2, e$) + Ar (panel (f)), together with the distributions that are expected from simulations of the experiment (black curves). Small segments of the distributions around forward scattering are masked by trace amounts of the reagent NO packet, and therefore marked by a gray box. The experimental scattering distribution is unreliable in this area. Panels (a) through (e) are adapted from ref.[21] with permission.

4 Prospects and challenges

The measurement of diffraction oscillations presented in the previous section is a testimony for the high image resolution facilitated by the Stark decelerator. Several possibilities exist to further increase the resolution of the images. At present, the resolution is mainly limited by the Rg atom beam, which has a much larger velocity spread than the packet of molecules emerging from the decelerator. The contribution of this velocity spread to the radial and angular distributions in the image depends on the beam crossing angle, and smart choices can be made to minimize the influence of the velocity spread. Still, a more narrow velocity and angular distribution of the collision partner will significantly improve the image resolution. This may be achieved by installing mechanical velocity selectors, for instance. Ultimately, however, one would like to achieve full control over both beams using molecular decelerators. This will also enable studies of bimolecular collision processes (*vide infra*).

The velocity and angular spread of the Stark-decelerated molecules can also be further reduced. At present, the velocity distribution is determined by the operation mode of the Stark decelerator (such as high voltage applied to the electrodes, the phase angle, and higher order resonance mode[25]), and by the dipole moment and mass of the molecular species. However, additional phase-space manipulation can be performed with the decelerated packet after the final velocity has been reached. Crompvoets *et al.* demonstrated that the last section of the decelerator can be used to rotate the longitudinal phase-space distribution of the decelerated molecules uniformly, such that the velocity distribution of the packet is compressed[29]. Using ND_3 molecules, the formation of molecular packets with a velocity spread of 0.76 m/s, corresponding to a temperature of 250 μK, has already been demonstrated with this technique.

The detection system itself can also be improved. More advanced VMI detectors, featuring electrostatic lenses that allow for time slicing[30,31] and zooming[32,33], have been developed in recent years. We expect that these state-of-the-art VMI techniques will significantly improve the resolution in our experiments as well.

By implementing one or more of the techniques outlined above, the resolution that may ultimately be obtained will allow us to study molecular collisions with sufficient detail to challenge the most sophisticated theoretical models for molecular interactions to date. There are many subjects that can be studied, in which the high resolution afforded by the combination of Stark deceleration and VMI can be used to advantage. The true potential of this best-of-both-worlds combination, however, lies in the study of phenomena that are difficult to address otherwise. In the following sections, we describe two such research perspectives as an example. In section 4.1 we describe the study of scattering at low collision energies, focusing on obtaining information on DCSs in the vicinity of scattering resonances. Section 4.2 describes the possibilities of studying collisions between two decelerated and state-

selected molecules, focusing on obtaining information on rotational product pairs for bimolecular inelastic collisions. In both case studies, we illustrate the possibilities using simulations of the expected scattering images. In these simulations, we conservatively use the molecular beam and imaging detector parameters that apply to the experimental results presented in this manuscript, i.e., for molecular velocity spreads and detector resolutions that have already been experimentally proven. The potential increase in resolution that may be obtained when improved beam sources, additional phase-space manipulation of the Stark-decelerated molecules, and/or improved VMI strategies are implemented, is not taken into account in these simulations. We follow the simulation methods as described in detail before [19–21].

4.1 Low collision energies

Recently, there has been a large interest in the study of molecular collisions at low collision energies. Cold collisions are governed by rich quantum phenomena foreign to high-energy collisions, such as tunnelling and scattering resonances [34]. Scattering resonances appear when the collision energy is resonant with the internal energy of a (quasi-) bound state of the collision complex, resulting in a sudden and dramatic increase in the collision cross section. Shape resonances are associated with tunnelling through the centrifugal barrier, whereas Feshbach resonances occur at energies around the energetic thresholds for excited states of the molecule. Both types of resonances are extremely sensitive to the exact topology of the molecular interaction [35].

Scattering resonances have proven difficult to observe experimentally [36,37]. Only recently, ingenious crossed beam arrangements resulted in the experimental observation of scattering resonances. For the benchmark F + HD reaction, resonance behaviour was observed in both integral [38] and differential cross sections [39]. Costes and coworkers used a crossed beam apparatus with variable crossing angle to measure scattering resonances in state-to-state integral cross sections for CO + H_2 [40] and O_2 + H_2 [41] collisions at energies down to a few cm^{-1}. Narevicius and coworkers designed a curved magnetic molecular guide, such that two molecular beams with almost equal velocity merge downstream from the guide, effectively producing a beam crossing angle near 0°. Cross sections for Penning ionization of metastable He with H_2, D_2 and HD could be measured at collision energies as low as 10^{-2} cm^{-1} [42,43]. In both types of experiments, scattering resonances were observed that reveal the contribution of individual partial waves to the scattering process.

The application of a Stark decelerator in a crossed beam experiment is well suited to reach the collision energies and energy resolutions required to measure scattering resonances. In addition, the Stark decelerator enables measurements of state-to-state DCSs at the resonances, where the narrow velocity spread prevents blurring of the angular distribution in these small low-energy images. This is illustrated here here using low-energy collisions of NH_3 molecules with He atoms as an example. The NH_3 molecule and its isotopologue ND_3 are amenable to the Stark deceleration technique, and have been employed frequently in deceleration experiments [44]. Gubbels *et al.* have predicted pronounced shape and Feshbach resonances for collisions between NH_3 molecules and He atoms [45]. In addition, dramatic changes are predicted to occur in the DCS at collision energies where a resonance is observed. For off-resonance collision energies, the DCS is mainly forward scattered and dominated by diffraction oscillations. When the collision energy is tuned to resonance, strong backward peaks appear in the DCS.

In Figure 10 we show the scattering images we expect to observe for the $|11-\rangle \rightarrow |11+\rangle$ inelastic scattering channel of NH_3 with He at collision energies of 30.0 and 37.28 cm^{-1}. At a collision energy of 37.28 cm^{-1}, a pronounced scattering resonance is predicted [45]. In the simulations we assume an experiment in which a Stark-decelerated packet of NH_3 molecules collides with a conventional beam of He atoms at a beam intersection angle of 45°. We assume that the He atom beam is produced using a cryogenic source that is maintained at a temperature of about 30 K, resulting in a He atom velocity of 550 m/s. Collision energies of 30.0 and 37.3 cm^{-1} are then obtained when the velocity of the NH_3 molecules is tuned to 655 and 742 m/s, respectively. We further assume velocity, spatial and temporal spreads for the NH_3 packet to be comparable to the spreads we have obtained in the experiments reported in this manuscript. For the He beam, we conservatively use a velocity spread of 55 m/s (FWHM) and an angular spread of 2.0° (FWHM). Furthermore, we assume that a recoil-free REMPI detection scheme can be used. The DCSs from Gubbels *et al.*, averaged over the expected collision energy distribution, are used as inputs to the simulations.

The images show that at these collision energies, we can still discern information about the DCS. By scanning the velocity of NH_3 with the Stark decelerator, the strong dynamic behaviour of the DCS as the collision energy is varied over resonances can be studied. The narrow velocity spread of the Stark-decelerated molecules will allow us to probe the interesting structure in the DCS predicted by theory. Such measurements yield additional insight in the dynamics of cold molecular collisions.

4.2 Product pair correlations in molecule-molecule scattering

Another interesting prospect of high image resolution is the possibility to study bimolecular collisions at the full state-selected level. An interesting aspect of bimolecular colli-

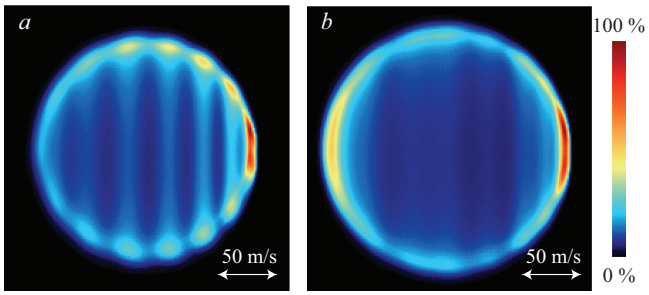

Fig. 10 Simulated scattering images for the $|11-\rangle \rightarrow |11+\rangle$ channel of NH_3 with He at collision energies of 30.0 cm^{-1} (a) and 37.28 cm^{-1} (b). At 30.0 cm^{-1} collision energy, the scattering distribution is dominated by diffraction oscillations. At a collision energy of 37.28 cm^{-1}, a pronounced Feshbach resonance is predicted resulting in a very different structure in the DCS.

sions is the possibility of rotational energy transfer in both molecules that take part in the encounter. Information on product pair correlations, i.e., the product state distribution of both molecules that are formed in coincidence from individual encounters, is most wanted to unravel the scattering dynamics in bimolecular collisions[12]. Surprisingly little is known about what happens at the ultimate quantum level when two state-selected molecules scatter with each other. *Ab initio* quantum scattering calculations are extremely challenging, and experimental data on bimolecular state-to-state cross sections is generally lacking.

Recently, the high quantum state purity of Stark-decelerated beams was used to perform the first inelastic collision experiment between two state-selected radical species[20]. A packet of state-selected and velocity controlled OH ($X\,^2\Pi_{3/2}, v = 0, j = 3/2, f$) radicals was formed by passing a beam of OH through a Stark decelerator. This packet was crossed with a hexapole state-selected beam of NO ($X\,^2\Pi_{1/2}, v = 0, j = 1/2, f$) radicals. State-resolved integral inelastic collision cross sections were measured by detecting the OH radicals using laser induced fluorescence. This experiment demonstrated that collision studies between two state-selected molecules are now feasible due to the state purity and associated product-state detection sensitivity afforded by Stark-decelerated beams.

When in such experiments the scattered molecules would be detected state-selectively using REMPI, and imaged via VMI, rotational product pairs could in principle be measured. Energy and momentum conservation results in concentric rings that reveal the final states of both species that are populated in coincidence from single collisions, yielding a kinematically complete picture of the scattering process[46]. These rings can be resolved using the narrow velocity spread of Stark-decelerated beams, as is illustrated below.

As a model system, consider a crossed beam scattering experiment between ^{14}NO and ^{15}NO radicals that are both prepared in the $X\,^2\Pi_{1/2}, v = 0, j = 1/2, f$ state prior to the collision. The two isotopologues are used to be able to spectroscopically discriminate between the species. The final state $X\,^2\Pi_{1/2}, v = 0, j = 3/2, e$ of the ^{14}NO molecules is probed using REMPI. Both beams intersect at a 90° crossing angle. In Figure 11, the scattering images are shown that are expected for three different situations, namely (*a*) the scattering of two conventional beams; (*b*) the scattering of a Stark-decelerated packet with a conventional beam; (*c*) the scattering of two Stark-decelerated packets. State selection of NO in a conventional beam is assumed to be obtained using a hexapole state selector, for instance. A mean velocity of 350 m/s is assumed for both beams. For the Stark-decelerated beams, we again use velocity, spatial and temporal spreads as before and for the conventional beams, we use a velocity spread of 35 m/s (FWHM) and an angular spread of 2.0° (FWHM). All energetically allowed scattering channels are taken into account in the simulations. Since we here merely illustrate the radial resolution that can be obtained, and since theoretical predictions for NO + NO collisions do not exist, we assume an isotropic DCS for all scattering channels. We further assume that the integral cross section for each scattering channel is such that each ring contributes with the same maximum intensity to the images.

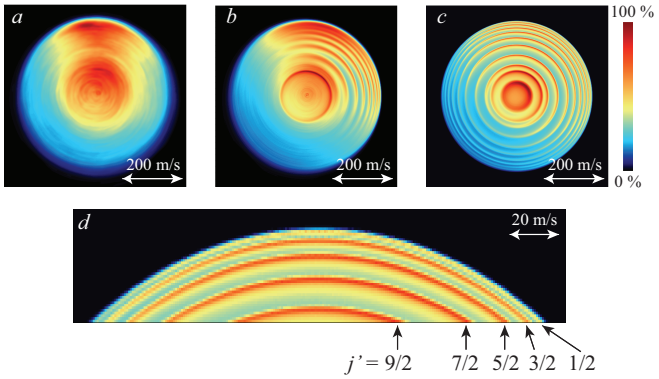

Fig. 11 Simulated scattering images for the scattering process ^{14}NO ($j = 1/2, f$) + ^{15}NO ($j = 1/2, f$) $\rightarrow$ ^{14}NO ($j = 3/2, e$) + ^{15}NO (j'). The images are simulated assuming a crossed beam experiment using (a) two conventional beams; (b) a Stark-decelerated packet and a conventional beam; (c) two Stark-decelerated packets. (d) Enlarged view of a section of image (c) showing the contribution of individual final states of ^{15}NO (j') to the image.

As can be seen from Figure 11, product pair correlations cannot be measured when two conventional beams are used. The NO radical has a rotational constant of 1.7 cm^{-1}, and the separation between the various rings is too small to be resolved. The multiple rings are partially resolved when a

Stark decelerator in combination with a conventional beam is used. Only when two decelerators are used, fully resolved sharp scattering rings appear, yielding full information on the state-to-state rotational product pairs. The rings that correspond to the various possible final rotational states j' of ^{15}NO are indicated in the enlarged view in panel *d*.

4.3 Challenges and limitations

The combination of Stark deceleration and VMI in scattering experiments can be used to advantage in a large variety of experiments; the examples described above illustrate a mere selection of possible future research directions. As with almost any other experimental approach, there are also limitations to the technique, and several challenges need to be overcome to fully exploit its potential. In this section, we give our opinion on the most important challenges and limitations.

Perhaps the most fundamental limitation of the technique is its limited chemical diversity. Stark deceleration can only effectively be used for species with a small mass and a large Stark shift in experimentally attainable electric fields. To date, the species that have been Stark-decelerated and that are most relevant to scattering experiments include OH ($X\,^2\Pi$), NH_3, NH ($a\,^1\Delta$), NO ($X\,^2\Pi$), CO ($a\,^3\Pi$), SO_2, LiH ($X\,^1\Sigma^+$), and H_2CO[16]. Although several others have been proposed, it will be challenging to apply the method to larger polyatomic molecules. The recent development of the related Zeeman deceleration technique[47–50] extends this chemical diversity to molecules like NH and O_2, H atoms, and all metastable atoms[51].

The feasibility of future experiments strongly depends on the densities of Stark-decelerated packets that can be reached, and the sensitivity with which scattered molecules can be probed. The operation of a Stark decelerator is based on the selection of a packet of molecules from the original molecular beam pulse. Therefore, the density of the decelerated packet is by definition lower than the density available in the molecular beam. This reduced density, however, has thus far not been a severe limitation, as it is accompanied by an increased quantum state purity. Generally, this results in reduced background levels in scattering experiments, compensating for the relatively low density. This was demonstrated in crossed beam scattering experiments between Stark-decelerated OH radicals and Rg atoms, where scattering processes with cross sections as low as 0.01 Å^2 could be observed[19,52]. This level of sensitivity is comparable to the sensitivity of conventional crossed beam experiments for similar systems. The densities, state-purities, and sensitivities reached thus far have even facilitated measurements of inelastic scattering cross sections between Stark-decelerated OH radicals and hexapole state-selected NO radicals[20]. Considering the observation that beams of OH are produced with relatively low intensities, the scattering of two Stark-decelerated beams appears feasible. In particular for species such as NH_3 and/or NO, we estimate that the product intensity is sufficient to measure rotational product pair correlations using VMI.

A technical challenge is presented by the need to probe the scattered molecules state-selectively using REMPI. Although for almost all species of interest REMPI schemes exist that are sensitive and relatively easy to implement, many of these schemes impart a large recoil energy to the ion. The corresponding recoil velocity can considerably reduce the image resolution. For a selection of relevant species, the most frequently used REMPI schemes are listed in Table 1, together with the recoil velocity imparted to the ion. For most species, recoil-free REMPI schemes have been demonstrated. However, their applicability to scattering experiments can be challenging due to reduced detection sensitivity of the scheme, the predissociative nature of intermediate electronic states and/or possible competition between various ionization pathways[53]. To fully exploit the high resolution afforded by the Stark decelerator for these species, the development of sensitive, state-selective and recoil-free REMPI schemes is essential.

5 Conclusions and outlook

In conclusion, the combination of the Stark deceleration method and VMI in crossed beam scattering experiments enables us to measure differential cross sections in molecular collisions with unprecedented resolution. This is illustrated by resolving quantum diffraction oscillations for inelastic collisions between NO radicals and rare gas atoms, which are among the most detailed structures that can occur in any DCS. Near-exact theoretical predictions for collision cross sections exist for these benchmark systems, and our experiments are fully consistent with the most accurate calculations presently possible. For less well-known systems, including bimolecular, polyatomic, or even reactive systems, our approach yields new possibilities to experimentally validate PESs and the approximations used to calculate them.

The improved image resolution afforded by molecular decelerator techniques fits into a long and rich history of efforts to measure state-to-state differential cross sections as accurately as possible. Although to the best of our knowledge we have obtained the highest resolution in velocity mapped ion images of a scattering process to date, we emphasize that high-resolution measurements of DCSs can be, and have been, obtained using conventional beam methods as well. For instance, diffraction oscillations and product pair correlations have already been measured for favorable systems in the 70's and 80's using ingenious high resolution scattering machines that employ rotatable detectors and time-of-flight methods[67–72]. Yet, the combination of advanced molecular beam methods and VMI as presented here offers fascinating perspectives for

Molecule	Excitation mechanism	Resonant transition	λ (nm)	Ion recoil (m/s)
NO	$1+1$	$A\,^2\Sigma^+ \leftarrow X\,^2\Pi$	$226+226$	14
	$1+1'$ [54]	$A\,^2\Sigma^+ \leftarrow X\,^2\Pi$	$226+328$	0
NH_3	$2+1'$ [55]	$\tilde{C}' \leftarrow \tilde{X}$	$287+560$	0*
	$2+1'$ [56]	$\tilde{B} \leftarrow \tilde{X}$	$317+435$	0
ND_3	$2+1$ [57]	$\tilde{B} \leftarrow \tilde{X}$	317	21
	$2+1'$ [58,59]	$\tilde{B} \leftarrow \tilde{X}$	328 + 455	0
OH	$2+1$ [60,61]	$3\,^2\Sigma^- \leftarrow X\,^2\Pi$	230	34
	$2+1$ [60–62]	$D\,^2\Sigma^- \leftarrow X\,^2\Pi$	244	26
	$1+1'$ [63]	$D\,^2\Sigma^- \leftarrow X\,^2\Pi$	122 + 434	0*
	$1+1'$ [64]	$A\,^2\Sigma^+ \leftarrow X\,^2\Pi$	282 + 118	unknown **
CO ($a\,^3\Pi$)	$1+1$ [65]	$b\,^3\Sigma^+ \leftarrow a\,^3\Pi$	283 + 283	10
	$1+1'$ ***	$b\,^3\Sigma^+ \leftarrow a\,^3\Pi$	283 + 345	0
NH ($a\,^1\Delta$)	$2+1$ [66]	$f\,^1\Pi \leftarrow a\,^1\Delta$	255	23

Table 1 Some commonly used state-selective REMPI schemes for selected species, detailing the resonant transition, laser wavelength(s) λ, and recoil velocity of the produced ion. * Excitation occurs to a high-lying Rydberg state followed by field ionization. ** The OH^+ ion is formed in an excited electronic state, and it is at present unclear how much recoil energy is imparted to ground state OH^+ ions. *** This scheme has to our knowledge never been demonstrated, but should be straightforward to implement.

novel state-to-state molecular beam collision experiments that go beyond resolving diffraction oscillations alone.

In the years to come, we envision that this combination of techniques can be used to advantage in a number of exciting research directions. In this manuscript, we have described two such directions in more detail; the study of collisions at low energies and the measurement of rotational product pairs for bimolecular inelastic collisions. But our approach is also well suited, for instance, to probe the alignment and orientation of product molecules [73,74]. Moreover, the study of inelastic and reactive scattering processes as a function of the collision energy allows for measurements of state-to-state DCSs around the energetic thresholds. We expect to observe interesting changes in the DCS as the collision energy is scanned from the energetic threshold to higher values. Obtaining additional control over the internal degrees of freedom of the reagent molecules is another exciting avenue. Sophisticated and novel laser-based methods are available nowadays to excite reagent molecules to selected rotational or vibrational states [75–79]. In combination with molecular beam deceleration methods, this would allow for complete control over the translational, rotational, and vibrational degrees of freedom of molecules, as well as their orientation or alignment in space.

As described so well by Levine and Bernstein decades ago, one of the ultimate goals in a molecular scattering experiment is to unravel the precise nature of molecular interactions by controlling all parameters of the encounter. Although the "ultimate" experiment does not exist, there has been a continuous and very successful effort by many groups to obtain ever better control over the relevant parameters. We hope and expect that the combination of molecular deceleration and imaging technology can play an important role in this development.

6 Acknowledgements

This work is part of the research program of the Foundation for Fundamental Research on Matter (FOM), which is financially supported by the Netherlands Organisation for Scientific Research (NWO). S.Y.T.v.d.M. acknowledges support from NWO via a VIDI grant, and from the European Research Council via a Starting Grant. S.Y.T.v.d.M. and D.H.P. thank NWO for financial support via a TOP grant. We thank the Fritz-Haber-Institute in Berlin for equipment loans. We thank Gerrit Groenenboom and Ad van der Avoird for continuous theoretical support and fruitful discussions. We thank Bethan Nichols for suggesting us the title of the manuscript. The expert technical support by Leander Gerritsen, Chris Berkhout, Peter Claus, Niek Janssen and André van Roij is gratefully acknowledged.

References

1 R. D. Levine and R. B. Bernstein, *Molecular reaction dynamics and chemical reactivity*, Oxford University Press, New York, 1987.
2 M. Brouard and C. Vallance, *Tutorials in Molecular Reaction Dynamics*, RSC Publishing, Cambridge, 2010.
3 R. B. Bernstein, *Science*, 1964, **144**, 141–150.
4 H. Kohguchi and T. Suzuki, *Annu. Rep. Prog. Chem., Sect. C*, 2002, **98**, 421.
5 P. Casavecchia, *Rep. Prog. Phys.*, 2000, **63**, 355–414.
6 X. Yang, *Annu. Rev. Phys. Chem.*, 2007, **58**, 433–459.
7 S. Stolte, *Nature*, 1991, **353**, 391–392.
8 J. Reuss, *Atomic and molecular beam methods*, Oxford University Press, New York, USA, 1988 & 1992, vol. 1 & 2, ch. 11, pp. 276–292.

9 S. Stolte, *Atomic and molecular beam methods*, Oxford University Press, New York, USA, 1988 & 1992, vol. 1 & 2, ch. 25, pp. 631–652.
10 H. Kohguchi, T. Suzuki and M. H. Alexander, *Science*, 2001, **294**, 832–834.
11 M. N. R. Ashfold, N. H. Nahler, A. J. Orr-Ewing, O. P. J. Vieuxmaire, R. L. Toomes, T. N. Kitsopoulos, I. A. Garcia, D. A. Chestakov, S.-M. Wu and D. H. Parker, *Phys. Chem. Chem. Phys.*, 2006, **8**, 26–53.
12 K. Liu, *Phys. Chem. Chem. Phys.*, 2007, **9**, 17.
13 N. E. Shafer-Ray, A. J. Orr-Ewing and R. N. Zare, *J. Phys. Chem.*, 1995, **99**, 7591.
14 A. T. J. B. Eppink and D. H. Parker, *Rev. Sci. Instrum.*, 1997, **68**, 3477–3484.
15 H. L. Bethlem, G. Berden and G. Meijer, *Phys. Rev. Lett.*, 1999, **83**, 1558–1561.
16 S. Y. T. van de Meerakker, H. L. Bethlem, N. Vanhaecke and G. Meijer, *Chemical Reviews*, 2012, **112**, 4828–4878.
17 S. Y. T. van de Meerakker, H. L. Bethlem and G. Meijer, *Nature Physics*, 2008, **4**, 595–602.
18 J. J. Gilijamse, S. Hoekstra, S. Y. T. van de Meerakker, G. C. Groenenboom and G. Meijer, *Science*, 2006, **313**, 1617–1620.
19 L. Scharfenberg, J. Kłos, P. J. Dagdigian, M. H. Alexander, G. Meijer and S. Y. T. van de Meerakker, *Phys. Chem. Chem. Phys.*, 2010, **12**, 10660.
20 M. Kirste, X. Wang, H. C. Schewe, G. Meijer, K. Liu, A. van der Avoird, L. M. C. Janssen, K. B. Gubbels, G. C. Groenenboom and S. Y. T. van de Meerakker, *Science*, 2012, **338**, 1060–1063.
21 A. von Zastrow, J. Onvlee, S. N. Vogels, G. C. Groenenboom, A. van der Avoird and S. Y. T. van de Meerakker, *Nat. Chem.*, 2014, **6**, 216–221.
22 D. W. Chandler and S. Stolte, in *Gas Phase Molecular Reaction and Photodissociation Dynamics*, ed. K. C. Lin and P. D. Kleiber, Transworld Research Network, 2007, ch. Inelastic energy transfer: The NO-rare gas system, pp. 1–63.
23 B. Yan, P. F. H. Claus, B. G. M. van Oorschot, L. Gerritsen, A. T. J. B. Eppink, S. Y. T. van de Meerakker and D. H. Parker, *Rev. Sci. Instrum.*, 2013, **84**, 023102.
24 L. Scharfenberg, H. Haak, G. Meijer and S. Y. T. van de Meerakker, *Phys. Rev. A*, 2009, **79**, 023410.
25 S. Y. T. van de Meerakker, N. Vanhaecke, H. L. Bethlem and G. Meijer, *Phys. Rev. A*, 2005, **71**, 053409.
26 W. Li, S. D. Chambreau, S. A. Lahankar and A. G. Suits, *Rev. Sci. Instrum.*, 2005, **76**, 063106.
27 X. Wang, M. Kirste, G. Meijer and S. Y. T. van de Meerakker, *Zeitschrift für Physikalische Chemie*, 2013, **227**, 1595–1604.
28 S. Y. T. van de Meerakker, N. Vanhaecke and G. Meijer, *Ann. Rev. Phys. Chem.*, 2006, **57**, 159–190.
29 F. M. H. Crompvoets, R. T. Jongma, H. L. Bethlem, A. J. A. van Roij and G. Meijer, *Phys. Rev. Lett.*, 2002, **89**, 093004.
30 D. Townsend, M. P. Minitti and A. G. Suits, *Rev. Sci. Instrum.*, 2003, **74**, 2530–2539.
31 J. J. Lin, J. Zhou, W. Shiu and K. Liu, *Rev. Sci. Instrum.*, 2003, **74**, 2495–2500.
32 Y. Zhang, C.-H. Yang, S.-M. Wu, A. van Roij, W. J. van der Zande, D. H. Parker and X. Yang, *Rev. Sci. Instrum.*, 2011, **82**, 013301.
33 H. L. Offerhaus, C. Nicole, F. Lépine, C. Bordas, F. Rosca-Pruna and M. J. J. Vrakking, *Rev. Sci. Instrum.*, 2001, **72**, 3245–3248.
34 D. W. Chandler, *J. Chem. Phys.*, 2010, **132**, 110901.
35 R. N. Zare, *Science*, 2006, **311**, 1383.
36 A. Schutte, D. Bassi, F. Tommasini and G. Scoles, *Phys. Rev. Lett.*, 1972, **29**, 979–982.
37 J. P. Toennies, W. Welz and G. Wolf, *J. Chem. Phys.*, 1979, **71**, 614–642.
38 R. T. Skodje, D. Skouteris, D. E. Manolopoulos, S.-H. Lee, F. Dong and K. Liu, *Phys. Rev. Lett.*, 2000, **85**, 1206–1209.
39 W. Dong, C. Xiao, T. Wang, D. Dai, X. Yang and D. H. Zhang, *Science*, 2010, **327**, 1501–1502.
40 S. Chefdeville, T. Stoecklin, A. Bergeat, K. M. Hickson, C. Naulin and M. Costes, *Phys. Rev. Lett.*, 2012, **109**, 023201.
41 S. Chefdeville, Y. Kalugina, S. Y. T. van de Meerakker, C. Naulin, F. Lique and M. Costes, *Science*, 2013, **341**, 1094–1096.
42 A. B. Henson, S. Gersten, Y. Shagam, J. Narevicius and E. Narevicius, *Science*, 2012, **338**, 234–238.
43 E. Lavert-Ofir, Y. Shagam, A. B. Henson, S. Gersten, J. Kłos, P. S. Żuchowski, J. Narevicius and E. Narevicius, *Nat. Chem.*, 2014, **6**, 332–335.
44 H. L. Bethlem and G. Meijer, *Int. Rev. Phys. Chem.*, 2003, **22**, 73–128.
45 K. B. Gubbels, S. Y. T. van de Meerakker, G. C. Groenenboom, G. Meijer and A. van der Avoird, *J. Chem. Phys.*, 2012, **136**, 074301.
46 J. J. Lin, J. Zhou, W. Shiu and K. Liu, *Science*, 2003, **300**, 966–969.
47 N. Vanhaecke, U. Meier, M. Andrist, B. H. Meier and F. Merkt, *Phys. Rev. A*, 2007, **75**, 031402(R).
48 S. D. Hogan, M. Motsch and F. Merkt, *Phys. Chem. Chem. Phys.*, 2011, **13**, 18705–18723.
49 E. Narevicius, A. Libson, C. G. Parthey, I. Chavez, J. Narevicius, U. Even and M. G. Raizen, *Phys. Rev. Lett.*, 2008, **100**, 093003.
50 E. Narevicius, A. Libson, C. G. Parthey, I. Chavez, J. Narevicius, U. Even and M. G. Raizen, *Phys. Rev. A*, 2008, **77**, 051401(R).
51 E. Narevicius and M. G. Raizen, *Chem. Rev.*, 2012, **112**, 4879–4889.
52 M. Kirste, L. Scharfenberg, J. Kłos, F. Lique, M. H. Alexander, G. Meijer and S. Y. T. van de Meerakker, *Phys. Rev. A*, 2010, **82**, 042717.
53 M. N. R. Ashfold and J. D. Howe, *Ann. Rev. Phys. Chem.*, 1994, **45**, 57–82.
54 J. B. M. Warntjes, F. Robicheaux, J. M. Bakker and L. D. Noordam, *J. Chem. Phys.*, 1999, **111**, 2556–2564.
55 J. A. Bacon and S. T. Pratt, *J. Chem. Phys.*, 2000, **113**, 7188–7196.
56 S. T. Pratt, *J. Chem. Phys.*, 2002, **117**, 1055–1067.
57 M. N. R. Ashfold, R. N. Dixon, R. J. Stickland and C. M. Western, *Chem. Phys. Lett.*, 1987, **138**, 201 – 208.
58 W. Habenicht, G. Reiser and K. Müller-Dethlefs, *J. Chem. Phys.*, 1991, **95**, 4809–4820.
59 H. Dickinson, D. Rolland and T. P. Softley, *J. Phys. Chem. A*, 2001, **105**, 5590–5600.
60 E. de Beer, M. P. Koopmans, C. A. de Lange, Y. Wang and W. A. Chupka, *J. Chem. Phys.*, 1991, **94**, 7634–7639.
61 M. E. Greenslade, M. I. Lester, D. C. Radenovic, A. J. A. van Roij and D. H. Parker, *J. Chem. Phys.*, 2005, **123**, 074309.
62 M. Collard, P. Kerwin and A. Hodgson, *Chem. Phys. Lett.*, 1991, **179**, 422 – 428.
63 C. McRaven, J. Alnis, B. Furneaux and N. Shafer-Ray, *J. Phys. Chem. A*, 2003, **107**, 7138–7141.
64 J. M. Beames, F. Liu, M. I. Lester and C. Murray, *J. Chem. Phys.*, 2011, **134**, 241102.
65 R. T. Jongma, G. Berden, T. Rasing, H. Zacharias and G. Meijer, *Chem. Phys. Lett.*, 1997, **273**, 147 – 152.
66 K. Wang, J. A. Stephens, V. McKoy, E. de Beer, C. A. de Lange and N. P. C. Westwood, *J. Chem. Phys.*, 1992, **97**, 211–221.
67 U. Buck, F. Huisken and J. Schleusener, *J. Chem. Phys.*, 1978, **68**, 5654–5655.
68 U. Buck, F. Huisken, J. Schleusener and J. Schaefer, *J. Chem. Phys.*, 1981, **74**, 535–544.
69 M. Faubel and G. Kraft, *J. Chem. Phys.*, 1986, **85**, 2671–2683.
70 U. Buck, F. Huisken, J. Schleusener and H. Pauly, *Phys. Rev. Lett.*, 1977, **38**, 680–682.
71 M. Faubel, K.-H. Kohl, J. P. Toennies, K. T. Tang and Y. Y. Yung, *Faraday Disc. Chem. Soc.*, 1982, **73**, 205–220.
72 U. Hefter, P. L. Jones, A. Mattheus, J. Witt, K. Bergmann and R. Schinke, *Phys. Rev. Lett.*, 1981, **46**, 915–918.

73 K. T. Lorenz, D. W. Chandler, J. W. Barr, W. Chen, G. L. Barnes and J. I. Cline, *Science*, 2001, **293**, 2063–2066.
74 M. Brouard, H. Chadwick, C. J. Eyles, B. Hornung, B. Nichols, F. J. Aoiz, P. G. Jambrina and S. Stolte, *J. Chem. Phys.*, 2013, **138**, 104310.
75 S. Yan, Y.-T. Wu, B. Zhang, X.-F. Yue and K. Liu, *Science*, 2007, **316**, 1723–1726.
76 B. L. Yoder, R. Bisson and R. D. Beck, *Science*, 2010, **329**, 553–556.
77 H. Chadwick, P. M. Hundt, M. E. van Reijzen, B. L. Yoder and R. D. Beck, *J. Chem. Phys.*, 2014, **140**, 034321.
78 W. Dong, N. Mukherjee and R. N. Zare, *J. Chem. Phys.*, 2013, **139**, 074204.
79 U. Gaubatz, P. Rudecki, S. Schiemann and K. Bergmann, *J. Chem. Phys.*, 1990, **92**, 5363–5376.
80 *Atomic and molecular beam methods*, ed. G. Scoles, Oxford University Press, New York, USA, 1988 & 1992, vol. 1 & 2.